


Please cite the Published Version

Regmi, YN  and Leonard, BM (2014) General synthesis method for bimetallic carbides of group VIIIA first row transition metals with molybdenum and tungsten. *Chemistry of Materials*, 26 (8). pp. 2609-2616. ISSN 0897-4756

DOI: <https://doi.org/10.1021/cm500076v>

Publisher: American Chemical Society (ACS)

Version: Accepted Version

Downloaded from: <https://e-space.mmu.ac.uk/624771/>

Additional Information: This is an Author Accepted Manuscript of an article published in *Chemistry of Materials* by ACS.

Enquiries:

If you have questions about this document, contact openresearch@mmu.ac.uk. Please include the URL of the record in e-space. If you believe that your, or a third party's rights have been compromised through this document please see our Take Down policy (available from <https://www.mmu.ac.uk/library/using-the-library/policies-and-guidelines>)

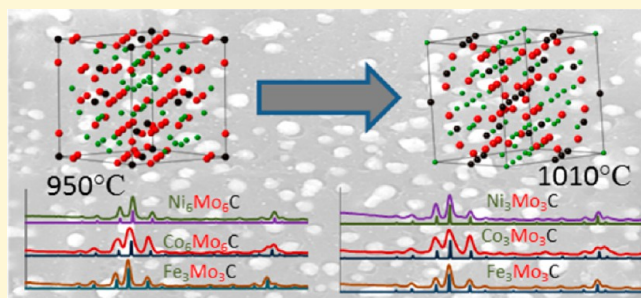
1 General Synthesis Method for Bimetallic Carbides of Group VIIIA First 2 Row Transition Metals with Molybdenum and Tungsten

3 Yagya N. Regmi and Brian M. Leonard*

4 Department of Chemistry, University of Wyoming, Laramie, Wyoming 82071, United States

5  Supporting Information

6 **ABSTRACT:** We have established a general method for the
7 synthesis of two different stoichiometries of bimetallic carbides
8 for each of the first row transition metals (TM) of Group
9 VIIIA with tungsten and molybdenum. A dispersion of
10 bimetallic carbide particles in a network of carbon was
11 achieved using excess carbon during the carbothermic
12 reduction process. An investigation into the reduction process
13 revealed bimetallic carbide formation proceeding via stepwise
14 reduction of oxide precursors to metals. The low carbon
15 content phase $\text{TM}_6(\text{Mo/W})_6\text{C}$ and the high carbon content
16 phase $\text{TM}_3(\text{Mo/W})_3\text{C}$ form within a temperature window of
17 60°C which emphasizes the need for careful control over reaction conditions in order to form the desired phase pure product.



18 ■ INTRODUCTION

19 Interest in transition metal (TM) carbides as alternative
20 catalytic materials for several chemical processes such as
21 oxygen reduction reaction (ORR), which typically involve rare
22 and expensive metals like platinum, has inspired numerous
23 investigations into their synthesis and development as
24 catalysts.¹ Tungsten carbide (WC) has been shown to catalyze
25 the formation of water at room temperature, which had not
26 been observed for any other TM besides platinum until the
27 tungsten carbide results were reported in 1973.² Since 1973,
28 catalytic activities were also observed, albeit in different
29 reactions, for various other metal carbides such as molybdenum
30 carbide (Mo_2C),³ iron carbide (Fe_3C),^{4,5} and cobalt carbide
31 (Co_2C).⁶ Efforts continue to be invested toward optimizing the
32 catalytic activities of monometallic carbides by fine-tuning the
33 electronic properties, morphology, and increasing the specific
34 surface area of various forms of these carbides.⁷

35 While TM carbides, such as molybdenum carbide, show
36 catalytic activities in reactions involving hydrogen transfer,^{8,9}
37 monometallic carbides tend to be unstable under catalytic
38 condition such as in proton exchange membrane (PEM) fuel
39 cells where the catalysts have to withstand highly reducing
40 environment and fluctuating voltage.¹⁰ WC specifically has
41 been proven to be unstable in such environments.¹¹ Efforts to
42 improve the stability include varying the stoichiometry of these
43 metal carbides, synthesizing polymorphs, and/or supporting
44 them on high surface area materials like carbon nanotubes and
45 silica.^{12,13} It has also been observed that the presence of a
46 second TM as either cemented material¹⁴ or as metal
47 nanoparticles supported on the carbide improve the stability
48 and activity of monometallic carbides like WC and Mo_2C .¹⁵

49 Increasing the surface area of the catalyst is the most popular
50 route toward optimization of the catalytic activity. However, it

has been shown that the mere presence of other TMs such as 51
iron and nickel into either tungsten or molybdenum carbide 52
lattice can also dramatically improve the catalytic activity of 53
these materials.^{16,17} The addition of a second TM into the 54
carbide lattice to form bimetallic carbides enables further tuning 55
of the electronic properties of the resulting material.¹⁸ 56
Additionally, cobalt molybdenum carbide was shown to be an 57
excellent alternative to carbon as a support material in ORR.¹⁹ 58
Thus, the synthesis of bimetallic carbides with various crystal 59
structures and stoichiometries is desirable to enhance the 60
investigation of metal carbides as advanced catalysts and/or 61
support materials. 62

Various methods have been utilized to synthesize bimetallic 63
carbides of the Group VIIIA metals—nickel, cobalt, and iron 64
with tungsten or molybdenum. Earliest attempts employed arc 65
melting that is energy expensive, due to the high temperatures 66
required, and long annealing time employed.²⁰ One of the 67
major drawbacks of the arc-melting bimetallic carbide products 68
is that they tend to have low specific surface area because of the 69
high temperatures employed. Temperature programmed 70
reduction carburization (TPRC) is another common method 71
that allows reduction of precursor materials at lower temper- 72
atures under a flow of hydrocarbon gases that serve as a source 73
of carbon.²¹ Although particle size of the TPRC product can be 74
reduced tremendously compared to the arc-melting method, 75
reproducibility and phase purity still have proven to be a 76
challenge.²² In most cases, the bimetallic carbide products 77
either contain monometallic carbides and elemental metals as 78
impurity or the second metal particles supported on the 79

Received: January 9, 2014

Revised: March 14, 2014

80 monometallic carbide crystals instead of being incorporated in
81 the crystal lattice itself. The latter case leads to the formation of
82 cemented carbides instead of bimetallic carbides.²³

83 Bimetallic carbides have also been prepared via various
84 intermediates that aid in size control and phase purity. Some of
85 the more successful routes have involved conversion of
86 bimetallic nitrides and oxides via calcination and intermetallic
87 alloys.²⁴ These methods tend to work for one particular
88 bimetallic carbide system to some extent, but not for others.
89 Specific synthesis methods involving highly specialized resins as
90 a source of carbon have also been reported for particular
91 bimetallic carbides of high purity and good activity.²⁵ No
92 common synthesis method that is energy efficient and simple
93 has been reported that can be employed to synthesize a broad
94 range of bimetallic carbides of TMs with molybdenum and
95 tungsten until now.

96 In this work, it is shown that a general method can be
97 employed for all three first row TMs in group VIIIA toward
98 formation of single phase bimetallic carbides of molybdenum
99 and tungsten. Additionally, we employ the same method to
100 prepare two different crystal structures for each system, with
101 high carbon content, $\text{TM}_3(\text{Mo}/\text{W})_3\text{C}$, and low carbon content,
102 $\text{TM}_6(\text{Mo}/\text{W})_6\text{C}$, by varying the annealing temperature the
103 samples are exposed to, i.e., the carbothermic reduction
104 temperature by 60 °C. This method utilizes stable oxide
105 precursors and relatively low carburization temperatures to
106 yield carbides with nanometer dimensions. Dispersion of
107 bimetallic carbide particles is also desirable to prevent
108 agglomeration of high surface area catalyst particles.²⁶ By
109 simply adding an excess of carbon, islands of bimetallic carbides
110 can be formed on a carbon support. Dispersed bimetallic
111 carbide particles were observed under scanning electron
112 microscope (SEM) for most systems, but reproducibility of
113 the phase pure bimetallic carbide was less consistent. To
114 overcome this phase separation, bimetallic oxides were
115 synthesized using a hydrothermal method and carburized
116 yielding bimetallic carbides with high specific surface area.^{27,28}
117 To probe the reduction of the precursor oxides and formation
118 of bimetallic carbides, the reactions were followed using a
119 thermogravimetric analysis instrument equipped with differ-
120 ential scanning calorimetry (TGA/DSC). The results showed
121 stepwise reduction of oxide precursors leading up to metals and
122 then the formation of bimetallic carbides. An investigation into
123 the transitions from low carbon content to high carbon content
124 phases revealed the complete decomposition of the carbide
125 phase and formation of intermetallic alloys of various
126 stoichiometries within the 60 °C temperature window.

127 ■ EXPERIMENTAL SECTION

128 **Materials.** NiO (99.8% <50 nm), Co_3O_4 (99.5% <50 nm), and
129 magnetite Fe_3O_4 (95% <5 μm) were used as received from Aldrich.
130 $\text{FeCl}_2 \cdot 2\text{H}_2\text{O}$ and $\text{NiCl}_2 \cdot 6\text{H}_2\text{O}$ were purchased from Mallinckrodt.
131 $\text{CoCl}_2 \cdot 6\text{H}_2\text{O}$ and decolorizing carbon were purchased from J. T.
132 Baker. $\text{Na}_2\text{MoO}_4 \cdot 2\text{H}_2\text{O}$ was purchased from Sigma, $\text{Na}_2\text{WO}_4 \cdot 2\text{H}_2\text{O}$
133 from Fisher Scientific, MoO_3 from Matheson Coleman & Bell as
134 $\text{H}_2\text{MoO}_4 \cdot \text{H}_2\text{O}$ containing 99% as MoO_3 , and $(\text{NH}_4)_6\text{H}_2\text{W}_{12}\text{O}_{40} \cdot x\text{H}_2\text{O}$
135 (99%) from Fluka. All the reagents were used as purchased except for
136 $(\text{NH}_4)_6\text{H}_2\text{W}_{12}\text{O}_{40} \cdot x\text{H}_2\text{O}$ (99%) which was placed inside a Thermo
137 Scientific Thermolyne Furnace (Benchtop Industrial/Type FD1500D)
138 in an alumina boat and heated to 650 °C for 5 h to obtain WO_3
139 powder.

140 **Carbothermic Reduction of Monometallic Oxides.** The metal
141 oxide powders represented by Fe_3O_4 (2.32×10^{-3} moles) and MoO_3
142 (6.95×10^{-3} mol) were combined with decolorizing carbon to

produce 1 to 1 molar ratio of the two metals and either stoichiometric
amount or 1 to 18 molar ratio of metal to carbon. The mixture was
ground with a mortar and pestle for 20 min to obtain a homogeneous
solid mixture. The resulting mixture was transferred to an alumina
crucible boat and heated in a furnace to the desired annealing
temperatures (AT). The annealing temperatures are detailed in Table
S1 (Supporting Information). The furnace was ramped to the
annealing temperatures at 1 °C/min under a flow of argon gas.
Once the highest temperature was achieved the tubes were rapidly
cooled down (15 °C/min) by opening the furnace lid and switching
off the power to the furnace. The resulting carburized sample was
ground to a fine powder for characterization.

Synthesis of Bimetallic Oxides. In a typical hydrothermal
synthesis of bimetallic oxide represented here by the iron molybdenum
system, 0.2 M aqueous solutions of FeCl_2 and $(\text{NH}_4)_2\text{MoO}_4$ were
prepared separately by stirring for 15 min. A total of 18 mL of each
solution was combined to achieve 80% volume of the reaction
chamber and stirred for an additional 15 min before adding to the
Teflon cup (45 mL) of an acid digestion vessel from Parr Instrument
Company. The acid digestion vessel was incubated at 180 °C for 24 h.
The precipitate was recovered by centrifugation and washed three
times with deionized water followed by three more times with ethanol.
Each washing cycle involved sonication of the sample for 15 min to
break up clumps and release soluble impurities prior to centrifugation.
The precipitate was dried at 50 °C for 2 h. Finally the product was
ground to a fine powder for characterization.

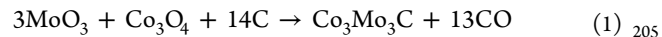
Carbothermic Reduction of Bimetallic Oxide. The as-
synthesized bimetallic oxide was combined with decolorizing carbon
such that the metal to carbon molar ratio was 1:18 and the mixture
ground for 15 min. The rest of the carburization process was
analogous to the process described for the reduction of the
monometallic oxides above in carbothermic reduction of monometallic
oxides.

Carbothermic Reduction in a TGA/DSC Furnace. Both
carbothermic reduction processes, with either monometallic or
bimetallic oxides, were studied in a TGA/DSC furnace to establish
the optimum carburization temperatures and ramping rates. Argon was
used as the flow gas at 100 mL/min.

Materials Characterization. X-ray diffraction (XRD) measure-
ments were performed on a Bruker-AXS Smart Apex II CCD
diffractometer equipped with an Oxford Cobra Cryosystem utilizing
Mo as the X-ray source. Thermogravimetric analysis (TGA) and the
corresponding differential scanning calorimetric (DSC) studies were
carried out on a SDTQ600 instrument from TA Instruments.
Brunauer–Emmett–Teller (BET) method was performed to
determine specific surface area on a Micromeritics ASAP2020
instrument using N_2 adsorption data at relative pressure from 0.05
to 0.25. Scanning electron microscopy (SEM) studies were carried out
on FEI Quanta FEG 450 field emission scanning electron microscope.
The SEM was equipped with a secondary electron detector, a
backscattered electron detector, and an Oxford Inca energy dispersive
X-ray detector (EDS). All SEM samples were deposited on a carbon
tape for analysis, and the acceleration voltage was 20 kV.

127 ■ RESULTS AND DISCUSSION

Bimetallic Carbides from Monometallic Oxides. Bimetallic carbides of W and Mo were synthesized by carbothermic reduction of individual metal oxides with decolorizing carbon. The oxides and carbon were ground together for 20 min to create a homogeneous mixture ensuring that carbothermic reduction can occur throughout the sample uniformly and produce a single phase product. Molar quantities of the oxides and carbon for all systems were based on eq 1.



The equimolar (TM) carbides of W and Mo occur primarily in two phases, $\text{TM}_3(\text{Mo}/\text{W})_3\text{C}$ and $\text{TM}_6(\text{Mo}/\text{W})_6\text{C}$. Since the precursor mole ratio of carbon to metal depends on which 208

209 product is formed, the highest carbon to metal ratio was
 210 selected as the ideal system to ensure complete reduction of
 211 oxides (Table S2, Supporting Information). The carburization
 212 reactions were carried out in an oxygen free argon environment,
 213 and thus, production of carbon monoxide as a byproduct is
 214 more likely than carbon dioxide. This also requires the highest
 215 carbon (C) to metal (M) ratio as shown in Table S2,
 216 Supporting Information, and was the basis for our precursor
 217 calculations.

218 After grinding, the precursors were annealed at various
 219 temperatures in an argon atmosphere to form the bimetallic
 220 carbide product. Surprisingly, the low carbon content bimetallic
 221 carbides of Fe, Co, and Ni and the corresponding high carbon
 222 content bimetallic carbides all form within the temperature
 223 window separated by 60 °C (Table S1, Supporting
 224 Information). This emphasizes the need for careful control
 225 over reaction conditions such as temperature, ramping rate,
 226 inert gas flow rate, and cooling rate, in order to form the
 227 desired phase pure product.

228 All the bimetallic carbides discussed here are based on a
 229 carbon face centered cubic (fcc) crystal lattice and have been
 230 classified eta (η) carbides. The only structural difference
 231 between the low carbon content and high carbon content
 232 carbides is that the high temperature bimetallic carbides contain
 233 twice the number of carbon atoms in the crystal lattice
 234 compared to low temperature bimetallic carbides. The
 235 increased number of carbon atoms slightly increases the lattice
 236 constants of the high carbon content structures. See Table S3
 237 (Supporting Information) for the lattice constants of the
 238 bimetallic carbides discussed in this work. This difference in
 239 lattice constant can be easily observed by XRD, especially at
 240 high angles, allowing reliable phase determination as seen in
 241 Figure S1 (Supporting Information).

242 Unlike in nickel and cobalt systems which yield $\text{Ni}_6\text{Mo}_6\text{C}$
 243 and $\text{Co}_6\text{Mo}_6\text{C}$, respectively, the corresponding $\text{Fe}_6\text{Mo}_6\text{C}$ phase
 244 is not observed in the iron system. The existence of the
 245 $\text{Fe}_6\text{Mo}_6\text{C}$ phase has been predicted²⁹ and claimed without
 246 significant evidence.^{30,31} It is also of note that the database used
 247 during our investigation, ICDD PDF-2 (2012), does not
 248 contain any references for the $\text{Fe}_6\text{Mo}_6\text{C}$ phase either. Our
 249 investigations reveal that cobalt and iron form the first
 250 bimetallic carbide ($\text{Co}_6\text{Mo}_6\text{C}$ and $\text{Fe}_3\text{Mo}_3\text{C}$, respectively)
 251 with molybdenum at 950 °C but nickel requires a slightly
 252 higher temperature of 975 °C. This behavior is consistent for
 253 the high carbon content phase $\text{Ni}_3\text{Mo}_3\text{C}$ as well. Cobalt and
 254 iron phases, $\text{Fe}_3\text{Mo}_3\text{C}$ and $\text{Co}_3\text{Mo}_3\text{C}$, form at 1010 °C, whereas
 255 $\text{Ni}_3\text{Mo}_3\text{C}$ is not observed until 1030 °C. Figure 1 shows the
 256 XRD patterns of the low carbon content (a) and high carbon
 257 content (b) bimetallic carbide phases of the three Group VIIIA
 258 first row TMs with molybdenum.

259 Contrary to previous attempts to synthesize bimetallic
 260 carbides of these three metals of Group VIIIA, our method
 261 yields single phase products for each system. To the best of our
 262 knowledge, all the methods reported until now are neither
 263 universal to all three first row group VIIIA TMs nor devoid of
 264 impurities. XRD spectra in Figure 1 show that our method can
 265 be employed to synthesize bimetallic carbides of all three TMs
 266 with molybdenum reproducibly, with little to no impurities.
 267 EDX analysis of the bimetallic carbides, shown in Table S4,
 268 Supporting Information, confirm the XRD results in Figure 1,
 269 showing that the two TMs involved are in equal atomic
 270 percentages throughout the sample. The uniform EDX data
 271 also decreases the probability of amorphous monometallic

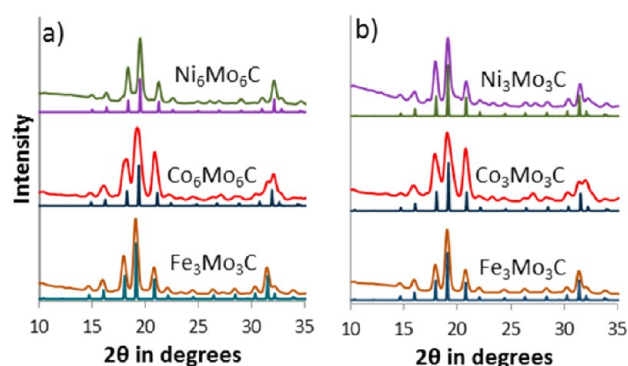


Figure 1. XRD patterns of low (a) and high (b) carbon content bimetallic carbide phases of Ni, Co, and Fe with Mo. The PDF card numbers for reference spectra are $\text{Ni}_6\text{Mo}_6\text{C}$ (04-005-5149), $\text{Co}_6\text{Mo}_6\text{C}$ (04-005-4048), $\text{Fe}_3\text{Mo}_3\text{C}$ (04-005-4038), $\text{Ni}_3\text{Mo}_3\text{C}$ (04-005-4042), and $\text{Co}_3\text{Mo}_3\text{C}$ (04-005-4043).

phases further supporting the determination that the products 272
 are single phase crystalline powders of bimetallic carbides. 273

The synthesis of bimetallic carbides of nickel was particularly 274
 challenging. Synthesis attempts based on as-obtained NiO 275
 resulted in nickel or nickel carbide impurities in addition to the 276
 target bimetallic carbide phase. NiO is the only well- 277
 characterized oxide of nickel and is green in color. However, 278
 NiO easily degrades to form nonstoichiometric oxides ranging 279
 in color from green to dark gray. Another commercially 280
 available oxide of nickel is Ni_2O_3 , which is a black non- 281
 stoichiometric oxide, and it contains a slightly higher 282
 percentage of nickel than the formula suggests.³² Since the 283
 as-obtained nickel oxide (NiO) was black in color, we assumed 284
 that it was Ni_2O_3 instead of NiO. In order to prepare phase 285
 pure bimetallic nickel carbide, a series of experiments with 286
 various mole ratios of nickel oxide to molybdenum oxide had to 287
 be carried out until neither metallic nickel nor nickel carbide 288
 formed. Once the stoichiometric adjustments in the precursor 289
 mixture were made from NiO to Ni_2O_3 , pure phase $\text{Ni}_6\text{Mo}_6\text{C}$ 290
 and $\text{Ni}_3\text{Mo}_3\text{C}$ were obtained on a consistent basis. 291

Synthetic routes to cobalt molybdenum carbides often 292
 produce a mixture of low carbon and high carbon content 293
 bimetallic carbide phases. As evident from Figure 1, the peaks 294
 on the XRD patterns for our cobalt systems are broader than 295
 that of iron and nickel bimetallic carbide systems. Such 296
 broadening has been previously assigned merely as impurity 297
 with very little discussion.^{25,33} This peak broadening could be 298
 due to either nanosized domains or the presence of a second 299
 bimetallic carbide phase. SEM data, discussed later, shows that 300
 the particle size for cobalt systems is comparable to iron and 301
 nickel systems, so the broadening observed cannot be assigned 302
 solely to smaller particle sizes based on the Scherrer Equation. 303
 The XRD peaks of $\text{Co}_3\text{Mo}_3\text{C}$ appear at slightly lower 2θ values 304
 than the corresponding peaks of $\text{Co}_6\text{Mo}_6\text{C}$, due to the increase 305
 in lattice constant of the former. Additionally, a careful 306
 observation of the two XRD peaks around 31° and 32° 2θ in 307
 Figure 1 shows that at lower temperature the XRD peak at 32° 308
 is taller (Figure 1a) while at higher temperature the two peaks 309
 become of almost similar intensity (Figure 1b). On the basis of 310
 lattice constants (Table S3, Supporting Information), it can be 311
 concluded that the relative proportion of $\text{Co}_3\text{Mo}_3\text{C}$ with higher 312
 lattice constant increases at higher temperature while the lower 313
 temperature phase is mostly composed of the smaller lattice 314
 constant phase, $\text{Co}_6\text{Mo}_6\text{C}$. 315

316 Formation of the corresponding bimetallic carbides of
 317 tungsten requires slightly higher temperatures (980 °C) relative
 318 to molybdenum systems (950 °C). Unlike the iron
 319 molybdenum system, the iron tungsten system occurs in both
 320 low carbon content ($\text{Fe}_6\text{W}_6\text{C}$) and high carbon content
 321 ($\text{Fe}_3\text{W}_3\text{C}$) phases. All three TMs Fe, Ni, and Co investigated
 322 here form phase pure low carbon content bimetallic carbides
 323 (Figure 2a). The high carbon content phases form at 60 °C

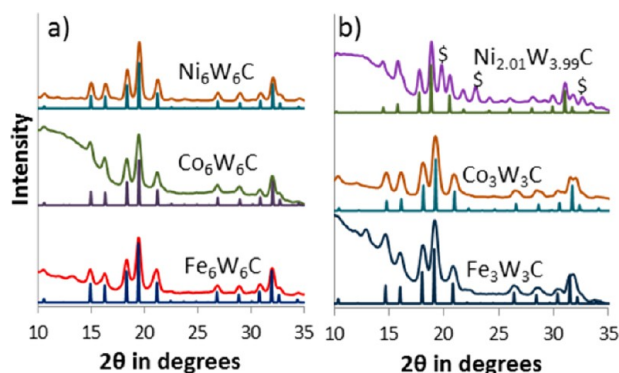


Figure 2. XRD patterns of low (a) and high (b) carbon content bimetallic carbide phases of Ni, Co, and Fe with W. The PDF card numbers for reference spectra are $\text{Ni}_6\text{W}_6\text{C}$ (04-005-4044), $\text{Co}_6\text{W}_6\text{C}$ (04-005-4045), and $\text{Fe}_6\text{W}_6\text{C}$ (04-005-4046), $\text{Ni}_{2.01}\text{W}_{3.99}\text{C}$ (04-005-4041), $\text{Co}_3\text{W}_3\text{C}$ (04-005-4040), and $\text{Fe}_3\text{W}_3\text{C}$ (04-005-4039).

324 higher than the low carbon content phase, analogous to the
 325 molybdenum systems. EDX mapping of the bimetallic carbides

with tungsten shown in Figure S2 (Supporting Information) 326
 show excellent overlap for the two constituent metals. 327

Iron forms phase pure $\text{Fe}_3\text{W}_3\text{C}$ and cobalt $\text{Co}_3\text{W}_3\text{C}$, but 328
 nickel repeatedly formed $\text{Ni}_{2.01}\text{W}_{3.99}\text{C}$ rather than the 329
 equimolar $\text{Ni}_3\text{W}_3\text{C}$. Despite adjusting the stoichiometry of 330
 the precursor oxides based on Ni_2O_3 as discussed above, phase 331
 pure $\text{Ni}_3\text{W}_3\text{C}$ could not be obtained. However, evidence of the 332
 formation of the $\text{Ni}_3\text{W}_3\text{C}$ phase can be seen (Figure S3, 333
 Supporting Information). The nickel tungsten carbide system 334
 has been studied in detail previously which revealed the 335
 existence of $\text{Ni}_6\text{W}_6\text{C}$ and $\text{Ni}_{2.01}\text{W}_{3.99}\text{C}$.³⁴ In addition to the 336
 anomalous stoichiometry of nickel tungsten carbide product, 337
 impurities in the form of Ni or NiC also persist, indicated by \$ 338
 in Figure 2b, even after adjusting the stoichiometry of the 339
 precursor oxides to yield $\text{Ni}_{2.01}\text{W}_{3.99}\text{C}$ instead of $\text{Ni}_3\text{W}_3\text{C}$. 340

Morphology and Particle Size Distribution. SEM 341
 analysis of the bimetallic carbide products reveals submicrom- 342
 eter particles in abundance for most of the tungsten systems, 343
 but the molybdenum systems in general have larger particle 344
 sizes (Figure 3). This can be attributed to the fact that the 345
 precursor molybdenum oxide has an average particle size of 346
 almost a micrometer (Figure S4a, Supporting Information) 347
 compared to in house prepared tungsten oxide which has 348
 particles ranging from 100 to 200 nm (Figure S4b, Supporting 349
 Information). Among the group VIIIA metal oxide precursors, 350
 Fe_3O_4 had much bigger particle size of almost a micrometer 351
 (Figure S4d, Supporting Information) compared to Co_3O_4 and 352
 NiO with particle sizes around 50 nm (Figures S4c,e, 353
 Supporting Information). Thus, our bimetallic carbides of 354
 iron molybdenum systems (Figures 3e,f) have comparatively 355
 bigger particle sizes compared to other systems. 356

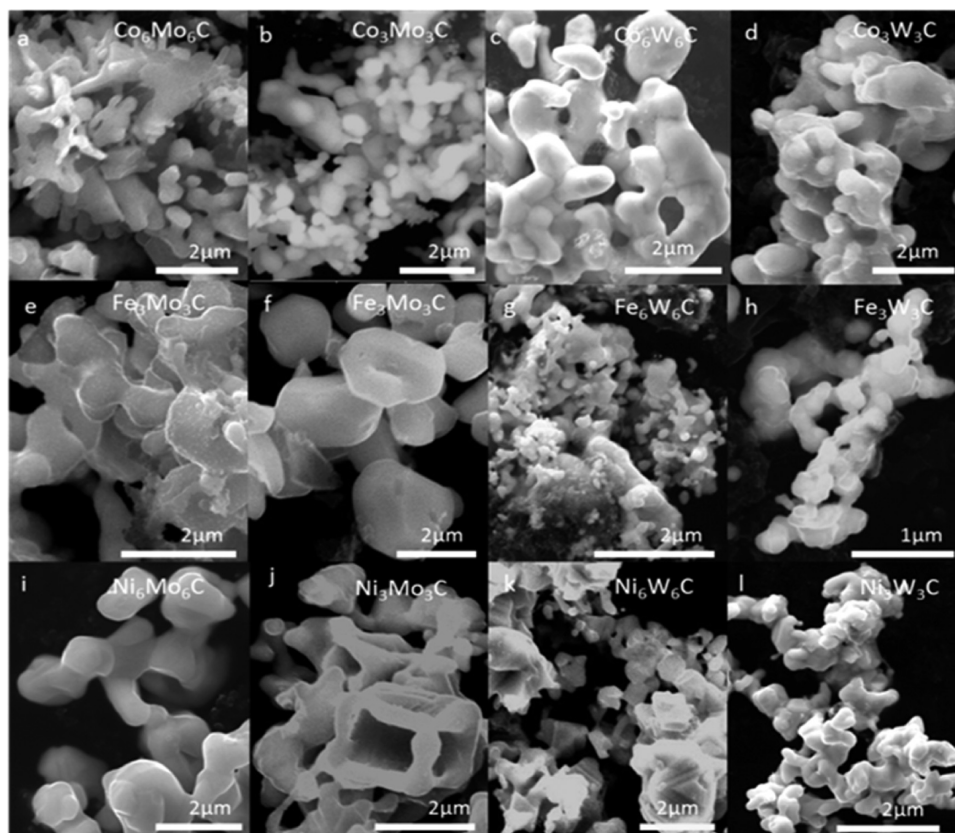


Figure 3. SEM images of various phases of bimetallic carbides of cobalt (a–d), iron (e–h), and nickel (i–l).

357 The most prevalent morphology is a network of spherical
 358 rods or dumbbells. Although there is variation of size within a
 359 sample from submicrometer to few micrometers (Figure 3b),
 360 there is a general uniformity in the morphology across this size
 361 variation. $\text{TM}_3\text{Mo}_3\text{C}$ systems show very different morphology
 362 and size among the three Group VIIIA metals. While Co–Mo–
 363 C (Figure 3a,b) mostly has spherical submicrometer particles
 364 dispersed with bigger dumbbell shapes, $\text{Fe}_3\text{Mo}_3\text{C}$ (Figure 3e,f)
 365 contains biconcave spheres up to a couple of micrometers in
 366 diameter. Ni–Mo–C (Figure 3i,j) contains a network of rods
 367 of few micrometers in length of submicrometer diameter.

368 A comparison of the low and high temperature samples of
 369 $\text{Fe}_3\text{Mo}_3\text{C}$ shows that the particles size is slightly bigger for the
 370 higher temperature 1010 °C sample (Figure 3f) compared to
 371 low temperature 950 °C (Figure 3e) sample. Although the
 372 crystal structure does not change unlike other systems, there is
 373 an observable increase in particle size even within 60 °C.

374 **Influence of Carbon Content on the Dispersion of the**
 375 **Bimetallic Carbides.** Catalyst nanoparticles frequently suffer
 376 from aggregation due to high surface energies. One common
 377 method to prevent nanoparticle agglomeration is to attach the
 378 catalyst material on a high surface area support like carbon. To
 379 achieve a dispersion of bimetallic carbide particles in a carbon
 380 network, an excess of carbon was used in the synthesis instead
 381 of the stoichiometric amount based on eq 1. During the course
 382 of the investigation, it was observed that an 18 molar excess
 383 achieves the optimum dispersion desired. Anything below the
 384 18 molar excess produces big clusters of bimetallic carbides
 385 while anything above it severely affects the reproducibility of
 386 the desired final product.

387 BET surface area of cobalt tungsten bimetallic carbides
 388 (Table S5, Supporting Information) shows an increase in the
 389 specific surface area from the stoichiometric sample 56 m^2/g to
 390 163 m^2/g upon the addition of excess carbon. While we cannot
 391 exclude the possibility of excess carbon being present in the
 392 stoichiometric samples, very little carbon is observed by SEM
 393 (Figure 3). The measured BET surface area of cobalt tungsten
 394 carbide samples with higher C:M is much higher due to the
 395 presence of a large amount of decolorizing carbon, which has a
 396 BET surface area of 585 m^2/g . Even though an accurate carbide
 397 surface area cannot be determined, the particle size is greatly
 398 decreased in the samples with excess carbon as seen in Figure 4
 399 further proving that the surface area of the bimetallic carbide is
 400 indeed increased.

401 When using 18 molar excess carbon, all the systems
 402 investigated here show the tendency to form dispersed arrays
 403 of bimetallic carbide particles on a carbon network to various
 404 degrees (Figure S5, Supporting Information). SEM analysis
 405 showed that the particle size of the bimetallic carbide is in the
 406 nanometer range in the dispersed form (Figure 4a) instead of
 407 clusters as observed in stoichiometric samples that have
 408 dimensions in micrometer range (Figure 4b). In addition,
 409 these smaller particles dispersed in carbon undergo less
 410 agglomeration because of the carbon network forming a barrier
 411 between particles.

412 Preliminary investigation shows that excess carbon produces
 413 a dispersed bimetallic array in all of our synthesized systems;
 414 however, the bimetallic particles are not dispersed homoge-
 415 neously in every sample. Large clusters of bimetallic carbides
 416 are present in some samples in addition to the dispersed
 417 moieties as in Figure S5e, Supporting Information. Additionally
 418 the bimetallic carbides are more difficult to obtain phase pure,
 419 unlike when stoichiometric amounts of carbon are used.

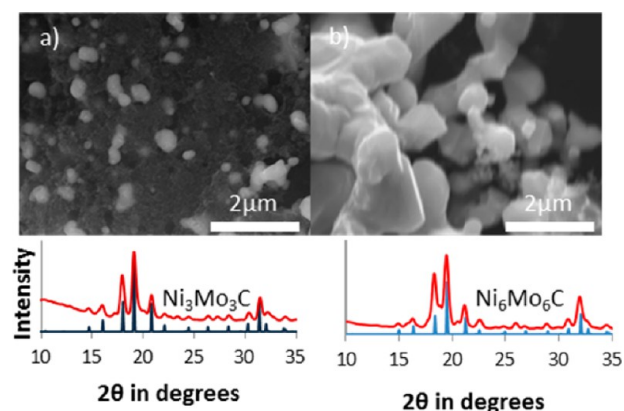


Figure 4. SEM images of bimetallic carbide phases of nickel molybdenum carbide with excess carbon content in starting material (a) and stoichiometric amount of carbon (b). The XRD graphs correspond to the SEM images above them.

420 It was also observed that a mixture of monometallic carbides
 421 were present in addition to the target, single phase bimetallic
 422 carbide. One possible explanation for this could be that the
 423 excess amount of carbon prevents the precursor oxides from
 424 being homogeneously distributed at close enough proximity to
 425 each other to react and form the bimetallic carbide. Instead the
 426 separation by excess carbon results in formation of mono-
 427 metallic carbides. Every sample, however, showed a majority of
 428 bimetallic carbide at the temperatures discussed previously.

429 **Synthesis of Bimetallic Carbides from Bimetallic**
 430 **Oxides.** One of the ways to circumvent phase separation in
 431 the dispersed carbide systems is to first produce nanopowders
 432 of corresponding bimetallic oxides and then use carbon to
 433 reduce the bimetallic oxides to bimetallic carbides. Zhen et al.
 434 in 2008 reported a one-step hydrothermal synthetic route for
 435 the preparation of CoWO_4 nanorods.²⁷ Others have reported
 436 the synthesis of tungstates and molybdates of other metals.^{35,36}
 437 The one-step hydrothermal method used for the synthesis of
 438 CoWO_4 nanorods was adopted to synthesize bimetallic oxides
 439 of the six systems discussed in our study, allowing the synthesis
 440 of the bimetallic carbide nanopowders.

441 Iron and cobalt molybdates are phase pure (Figure 5a), but
 442 similar purity in nickel molybdate could not be obtained using

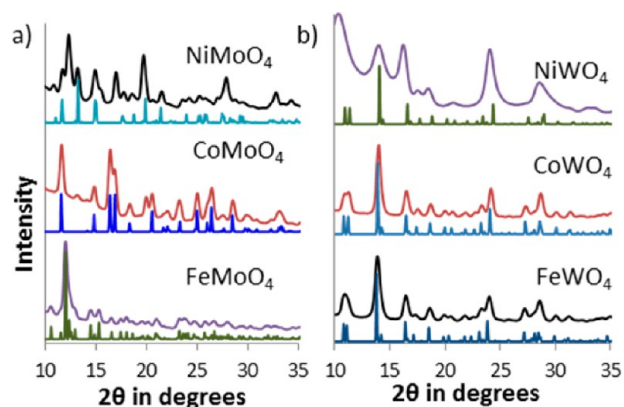


Figure 5. XRD patterns of bimetallic oxide phases, synthesized via solvothermal method, of Ni, Co, and Fe with Mo (a) and W (b). The PDF card numbers for reference spectra are NiMoO_4 (00-033-0948), $\text{Co}_3\text{Mo}_3\text{O}_8$ (01-078-7234), FeMoO_4 (01-089-267), NiWO_4 (00-015-0755), CoWO_4 (00-015-0867), and FeWO_4 (00-046-1446).

443 our hydrothermal method; however, other methods have been
 444 employed previously to synthesize phase pure NiMoO_4 .³⁵
 445 Although nickel molybdate was in the final product, MoO_3 and
 446 NiO were present as impurities in noticeable quantities (Figure
 447 5a). The ratio of the peaks in the experimental diffraction
 448 pattern is slightly different from that of the reference spectra for
 449 both nickel and cobalt tungstate (Figure 5b), indicating
 450 preferential growth similar to what Zhen et al. reported. In
 451 nickel tungstate, the XRD peaks at 17° and 25° are of similar
 452 intensity to the peak at 12° . In the reference spectra the XRD
 453 peak at 12° is twice the intensity of the ones at 17° and 25° . In
 454 cobalt tungstate, the peak at 29° is taller than the peak at 27° in
 455 the experimental data, whereas the two peaks are of the same
 456 intensity in the reference diffraction pattern (Figure 5b).
 457 Surprisingly, although nickel molybdate is the least phase
 458 pure of the three molybdate systems, the corresponding carbide
 459 of nickel is the most phase pure of the three systems we
 460 synthesized (Figure 6a). Essentially, this reasserts the simplicity

f6

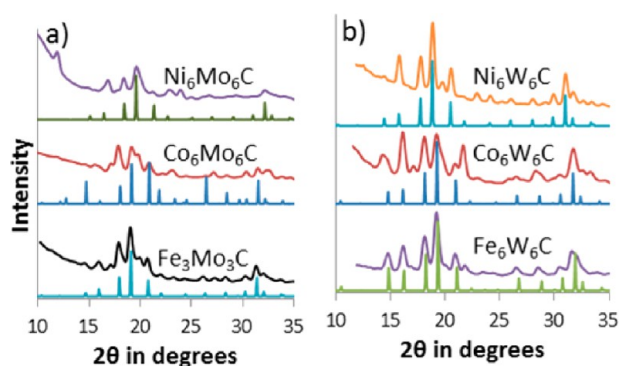


Figure 6. XRD patterns of bimetallic carbide phases, prepared by carburizing the corresponding bimetallic oxides, synthesized via solvothermal method, of Ni, Co, and Fe with Mo (a) and W (b).

461 of obtaining phase pure bimetallic carbides from individual
 462 oxides as in Figures 1 and 2. Most of the samples obtained via
 463 bimetallic oxides contain primarily bimetallic carbide, although
 464 the impurities in the form of metals such as iron or nickel,
 465 intermetallic alloys such as Ni_4Mo , or monometallic carbides
 466 such as Mo_2C are observable by XRD as seen in Figure 6. The
 467 broadness of the peaks in the cobalt molybdenum carbide XRD
 468 pattern in Figure 6b again shows the tendency to produce a
 469 mixture of low carbon content and high carbon content
 470 bimetallic carbide phases. Iron molybdenum carbide from
 471 bimetallic oxide contains metallic iron impurity indicated by the
 472 XRD peak at 19° . Nickel tungsten carbide has some nickel
 473 impurity as indicated by the XRD peak at 20° . Iron tungsten
 474 carbide is relatively phase pure, but cobalt tungsten carbide
 475 synthesized from bimetallic oxide tends to suffer the most
 476 among tungsten systems and produces a significant amount of
 477 cobalt carbide impurity (Figure 6b).

478 Our bimetallic oxide route, however, did not result in the
 479 dispersion of the bimetallic carbide that was observed with the
 480 18 molar excess of carbon from monometallic oxide synthesis
 481 route as seen in SEM images in Figure 7. The EDX maps show
 482 complete overlap of the two constituent TMs verifying the
 483 bimetallic carbide, but in spite of the bimetallic oxide and
 484 carbon mixture having 18 molar carbon excess, there is very
 485 little evidence from SEM of nanoparticle dispersion in the
 486 carbon network. The temperatures required for formation of

f7

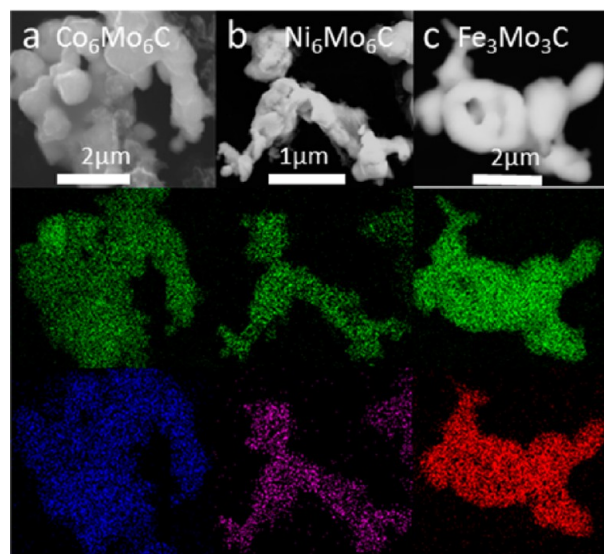


Figure 7. EDX mapping low carbon content bimetallic carbide phases of $\text{Co}_6\text{Mo}_6\text{C}$ (a), $\text{Ni}_6\text{Mo}_6\text{C}$ (b), and $\text{Fe}_3\text{Mo}_3\text{C}$ (c). Green map corresponds to molybdenum while blue, purple, and red correspond to cobalt, nickel, and iron, respectively.

bimetallic carbide via the bimetallic oxide route and
 monometallic oxide route are the same.

Reduction Pathway from Monometallic Oxide to Bimetallic Carbide. To better understand the reduction pathway for precursor oxides, the formation of cobalt molybdenum carbide was investigated by XRD and TGA/DSC as seen in Figure S6 (Supporting Information) and Figure 8, respectively. Although the reduction process for TPR

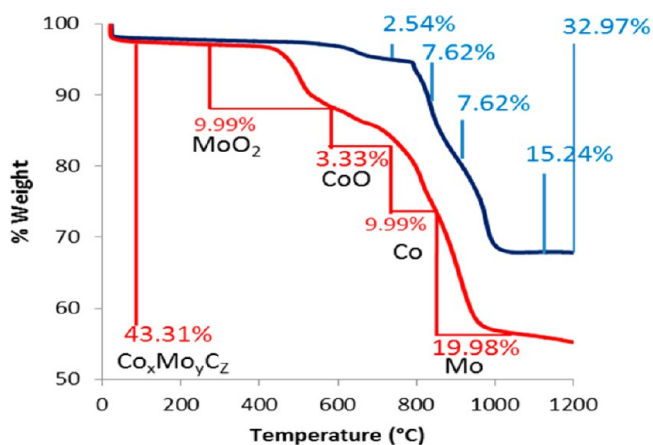


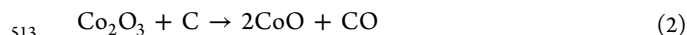
Figure 8. TGA curve for the reduction of a mixture of Co_3O_4 and MoO_3 (lower curve) and Co_3O_4 and WO_3 (upper curve).

reactions of monometallic carbides such as Mo_2C ^{37,38} and WC ³⁹ have been investigated before, we wanted to gain greater insight into the formation pathway for bimetallic carbides under our reaction conditions.

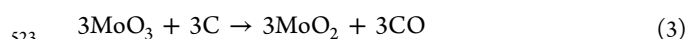
The TGA curves in Figure 8 below and equations from Table S2 (Supporting Information) show that carbon monoxide is the most likely byproduct, instead of carbon dioxide. The TGA graphs also provide an insight into the reduction pathway.

The total mass losses for both molybdenum and tungsten systems represented in Figure 8 are in excellent agreement with the theoretical mass losses based on eq 1 and the

506 corresponding equation for tungsten system. Co_3O_4 is a mixed
 507 valence oxide of cobalt with Co(II) and Co(III) present. From
 508 Table S6 (Supporting Information),⁴⁰ the electrochemical
 509 reduction potentials of each reduction step would suggest
 510 that Co(III) would be reduced to Co(II) resulting in a loss of
 511 one mole of CO represented by eq 2, which corresponds to
 512 3.33% mass loss.

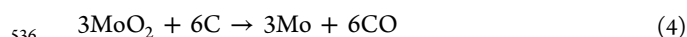


514 This same event represented by eq 2 should occur
 515 analogously in the tungsten system as well. However, the first
 516 mass loss event on the molybdenum curve corresponds to a
 517 loss of 3 mol of carbon monoxide around 500 °C. It is more
 518 likely that the reaction in eq 2 occurs around 625 °C because a
 519 mass loss event on the tungsten curve around the same
 520 temperature corresponds to the loss of one CO as well. It is
 521 more likely that the first thermal event is represented by eq 3.
 522 The mole numbers are retained from eq 1 for consistency.



524 Since reduction of Mo(VI) to Mo(IV) takes place before the
 525 thermodynamically favored reduction of Co(III) to Co(II) this
 526 step must be kinetically favored. Reduction of MoO_3 before
 527 Co_2O_3 was further confirmed by XRD (Figure S6, Supporting
 528 Information). At 525 °C, the XRD peak at 12° 2θ
 529 corresponding to MoO_3 disappears while the peak at 14°
 530 (Co_3O_4) persists, confirming our hypothesis that MoO_3 is
 531 reduced first.

532 Similarly, kinetics favors reduction of MoO_2 to Mo before
 533 CoO to Co whereas reduction potentials dictate that the
 534 appearance of molybdenum metal should precede the
 535 appearance of cobalt.



538 From the TGA graph it is apparent that the three carbon
 539 monoxide loss events at approximately 750 °C precedes the six
 540 carbon monoxide loss events starting around 850 °C. The XRD
 541 peak at 20° which is unique to cobalt metal in the graph (Figure
 542 S6, Supporting Information) is present at 775 °C but the XRD
 543 peak at 18° which is unique to molybdenum appears only at
 544 825 °C. The Mo reduction temperature is consistent with TPR
 545 studies observed during the formation of Mo_2C .³⁸

546 The XRD data also supports the gradual buildup of metallic
 547 alloy before the formation of bimetallic carbide based on the
 548 XRD peak at 21° corresponding to the Mo–Co alloy. The fact
 549 that the XRD peak at 21° (€ symbol) grows in relative intensity
 550 compared to the XRD peak at 20° (@ symbol), representative
 551 of metallic cobalt, suggests that proportion of the alloy is
 552 increasing and metallic cobalt decreasing.

553 **Transition from Low Carbon Content to High Carbon**
 554 **Content Phases.** In order to probe the transition from the low
 555 carbon content phase to high carbon content phase, we studied
 556 the intermediate temperatures by XRD. Not only did the low
 557 and high carbon content phases form at temperatures separated
 558 by only 60 °C, the transitions proceeded via formation of
 559 intermetallic alloy intermediates as shown in Figure 9. Thus it
 560 can be concluded that, instead of additional carbon atoms
 561 simply inserting into the low carbon content bimetallic carbide
 562 crystal lattice, the low carbon content crystal phase completely
 563 decomposes and reforms capturing more carbon atoms to form
 564 high carbon content crystal structure.

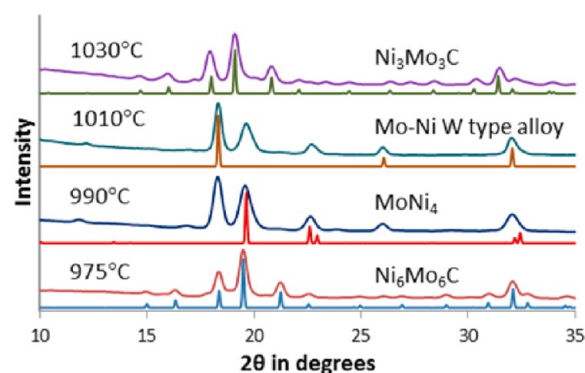


Figure 9. XRD patterns depicting the transition of bimetallic carbide phases of Ni from low carbon content phases to high carbon content phase. The PDF card numbers for reference spectra are $\text{Ni}_6\text{Mo}_6\text{C}$ (01-005-5149), MoNi_4 (00-003-1036), Mo–Ni W type alloy (01-071-9769), and $\text{Ni}_3\text{Mo}_3\text{C}$ (04-005-4042).

565 All of the TM carbides underwent the transformation from
 566 low to high via the same mechanism. The low carbon content
 567 bimetallic carbide phase separates into intermetallic alloys
 568 before the emergence of the high carbon content phase.
 569 Bimetallic carbides are known to phase separate into
 570 intermetallic alloys and/or monometallic carbides at temper-
 571 atures beyond their formation temperatures.⁴¹ As an example of
 572 the reaction mechanism from low to high carbon content
 573 bimetallic carbide, $\text{Ni}_6\text{Mo}_6\text{C}$ forms at 975 °C, but by 990 °C
 574 the product phase separates into a mixture of a nickel rich alloy
 575 (MoNi_4) and molybdenum rich alloy Mo–Ni (W type
 576 structure). Mo–Ni W type alloy in the nickel system used in
 577 Figure 9 is 98% molybdenum.⁴² The stoichiometry in the
 578 reference spectra was picked to match the experimental spectra
 579 as the reference work listed the value of x in $\text{Mo}_x\text{Ni}_{1-x}$ from
 580 0.985 to 1. These alloys then react with available carbon and
 581 reform a metal carbide phase with higher carbon content at
 582 1030 °C.

583 The temperature dependent fluctuation between bimetallic
 584 carbides and intermetallic alloys of various stoichiometries
 585 continues beyond the temperatures relevant to our synthesis. In
 586 our investigations beyond 1040 °C, we have observed
 587 bimetallic carbides of both low and high carbon content type
 588 also forming at higher temperatures (Figure S7, Supporting
 589 Information). It can be seen that the iron tungsten carbide
 590 system forms high carbon content bimetallic phase at 1060 °C
 591 and low carbon content phase at 1100 °C. However, these
 592 higher temperature phases are relatively less phase pure and
 593 contain monometallic carbide impurities such as tungsten
 594 carbide. As apparent from Figure S7 (Supporting Information),
 595 the high carbon content and low carbon content phases do not
 596 form at corresponding lower and higher temperatures unlike
 597 the two iron–tungsten phases reported in this investigation at
 598 980 and 1040 °C. The temperatures quoted for our synthesis
 599 here represent the lowest temperatures where the low and high
 600 carbon content bimetallic carbides can be formed using our
 601 method.

602 ■ CONCLUSIONS

603 We have demonstrated that a common synthesis route can be
 604 employed to synthesize bimetallic carbides of Group VIIIA
 605 metals with molybdenum and tungsten. Additionally, we have
 606 proved that within each system there exist bimetallic carbide
 607 phases with high $\text{TM}_3(\text{Mo}/\text{W})_3\text{C}$ and low $\text{TM}_6(\text{Mo}/\text{W})_6\text{C}$

608 carbon contents. The formation of these two phases occurs at
609 temperatures separated by as little as 60 °C. This emphasizes
610 the need to carefully control experimental parameters such as
611 annealing temperature, dwelling time, inert gas flow rate,
612 grinding duration, source of carbon, and ramping rate to
613 improve reproducibility. Utilizing TGA and XRD, an
614 investigation into the reduction route of the precursor oxide
615 revealed that the reduction reaction occurs in a stepwise
616 fashion. We also demonstrate the distribution, size, and
617 morphology of the bimetallic carbide particles can be controlled
618 by varying the carbon content in the precursor mixture which
619 may provide a basis to improve catalyst stability.

620 ■ ASSOCIATED CONTENT

621 ● Supporting Information

622 Additional tables and figures. This material is available free of
623 charge via the Internet at <http://pubs.acs.org>.

624 ■ AUTHOR INFORMATION

625 Notes

626 The authors declare no competing financial interest.

627 ■ ACKNOWLEDGMENTS

628 We would like to thank the University of Wyoming for start-up
629 funds and the School of Energy Resources for funding.

630 ■ REFERENCES

- 631 (1) Zhou, X.; Qiu, Y.; Yu, J.; Yin, J.; Gao, S. *Int. J. Hydrogen Energy*
632 **2011**, *36*, 7398.
633 (2) Levy, R. B.; Boudart, M. *Science* **1973**, *181*, 547.
634 (3) Lee, J. J. *Catal.* **1987**, *106*, 125.
635 (4) Eckstrom, H. C.; Adcock, W. A. *J. Am. Chem. Soc.* **1950**, *72*, 1042.
636 (5) He, Z.; Maurice, J.-L.; Gohier, A.; Lee, C. S.; Pribat, D.; Cojocaru,
637 C. S. *Chem. Mater.* **2011**, *23*, 5379.
638 (6) Weller, S.; Hofer, L. J. E.; Anderson, R. B. *J. Am. Chem. Soc.* **1948**,
639 *70*, 799.
640 (7) Alexander, A. M.; Hargreaves, J. S. *Chem. Soc. Rev.* **2010**, *39*,
641 4388.
642 (8) *The Chemistry of Transition Metal Carbides and Nitrides*, 1st ed.;
643 Oyama, S. T., Ed.; Blackie Academic & Professional: Glasgow, 1996.
644 (9) Lee, J. S.; Locatelli, S.; Oyama, S. T.; Boudart, M. *J. Catal.* **1990**,
645 *125*, 157.
646 (10) Barbir, F. *PEM Fuel Cells*, 2nd ed.; Academic Press: London,
647 2013.
648 (11) Zhang, J.; Tang, S.; Liao, L.; Yu, W. *Chin. J. Catal.* **2013**, *34*,
649 1051.
650 (12) Volpe, L.; Boudart, M. *J. Solid State Chem.* **1985**, *59*, 332.
651 (13) Da Costa, P.; Lemberon, J.-L.; Potvin, C.; Manoli, J.-M.; Perot,
652 G.; Breyse, M.; Djega-Mariadassou, G. *Catal. Today* **2001**, *65*, 195.
653 (14) Scholl, H.; Hofman, B.; Rauscher, A. *Electrochim. Acta* **1992**, *37*,
654 447.
655 (15) Mohan, K.; Strutt, P. R. *Nanostruct. Mater.* **1996**, *7*, 547.
656 (16) Xiao, T. *J. Catal.* **2002**, *209*, 318.
657 (17) Puello-Polo, E.; Brito, J. L. *J. Mol. Catal. A: Chem.* **2008**, *281*, 85.
658 (18) Liu, Y.; Kelly, T. G.; Chen, J. G. G.; Mustain, W. E. *ACS Catal.*
659 **2013**, *3*, 1184.
660 (19) Ma, X.; Meng, H.; Cai, M.; Shen, P. K. *J. Am. Chem. Soc.* **2012**,
661 *134*, 1954.
662 (20) Fraker, A. C.; Stadelman, H. *Trans. Metall. Soc. AIME* **1969**, *245*,
663 847.
664 (21) Volpe, L.; Boudart, M. *J. Solid State Chem.* **1985**, *59*, 348.
665 (22) Alconchel, S.; Sapina, F.; Martinez, E. *Dalton Trans.* **2004**, 2463.
666 (23) Michalski, A.; Siemiaszko, D. *Int. J. Refract. Met. Hard Mater.*
667 **2007**, *25*, 153.
668 (24) Korlann, S.; Diaz, B.; Bussell, M. E. *Chem. Mater.* **2002**, *14*,
669 4049.

- (25) Wang, X.-H.; Zhang, M.-H.; Li, W.; Tao, K.-Y. *Catal. Today* **2008**, *131*, 111. 670
671
(26) Shao, Y.; Yin, G.; Gao, Y. *J. Power Sources* **2007**, *171*, 558. 672
(27) Zhen, L.; Wang, W.-S.; Xu, C.-Y.; Shao, W.-Z.; Qin, L.-C. *Mater.* 673
Lett. **2008**, *62*, 1740. 674
(28) Moura, A. P. d. *Adv. Chem. Eng. Sci.* **2012**, *02*, 465. 675
(29) Goldschmidt, H. J. *Interstitial Alloys*; Butterworths: London, 676
1967. 677
(30) Lad'yanov, V. I.; Sterkhova, I. V.; Kamaeva, L. V.; Chueva, T. R.; 678
Molokanov, V. V. *J. Non-Cryst. Solids* **2010**, *356*, 65. 679
(31) Mccandlish, L. E.; Kugler, E. L.; Jacobson, A. J.; Chianelli, R. R. 680
Google Patents, 1994. 681
(32) Greenwood, N. N. *Chemistry of the elements*, 2nd ed.; 682
Butterworth-Heinemann: 1984. 683
(33) Xiao, T. *J. Catal.* **2001**, *202*, 100. 684
(34) Cury, R.; Joubert, J. M.; Tusseau-Nenez, S.; Leroy, E.; Allavena- 685
Valette, A. *Intermetallics* **2009**, *17*, 174. 686
(35) Chen, M.; Wu, J.-L.; Liu, Y.-M.; Cao, Y.; Guo, L.; He, H.-Y.; 687
Fan, K.-N. *J. Solid State Chem.* **2011**, *184*, 3357. 688
(36) Shim, H. W.; Cho, I. S.; Hong, K. S.; Cho, W. I.; Kim, D. W. 689
Nanotechnology **2010**, *21*, 465602. 690
(37) Oyama, S. T. *Catal. Today* **1992**, *15*, 179. 691
(38) Guil-López, R.; Nieto, E.; Botas, J. A.; Fierro, J. L. G. *J. Solid* 692
State Chem. **2012**, *190*, 285. 693
(39) Löfberg, A.; Frennet, A.; Leclercq, G.; Leclercq, L.; Giraudony, 694
J. M. *J. Catal.* **2000**, *189*, 170. 695
(40) *Standard Potentials in Aqueous Solution*; Bard, A. J., Parsons, R., 696
Jordan, J., Eds.; Marcel Dekker, Inc.: New York, 1985. 697
(41) Dubrovinskaia, N. A.; Dubrovinsky, L. S.; Saxena, S. K.; Selleby, 698
M.; Sundman, B. *Journal of Alloys and Compounds* **1999**, *285*, 242. 699
(42) Harker, D. J. *Chem. Phys.* **1944**, *12*, 315. 700